Proceedings of Proceedings of the International Design Engineering Technical Conferences & Computers & Information in Engineering Conference
IDETC/CIE 2023
August 17-20, 2023, Virtual Conference, USA

IDETC2023-116342

DESIGNING PROGRAMMABLE FERROMAGNETIC SOFT METASTRUCTURES FOR MINIMALLY INVASIVE ENDOVASCULAR THERAPY

Ran Zhuang[1], Jiawei Tian[1], Apostolos Tassiopoulos[2], Chander Sadasivan[3], Xianfeng Gu[4,5], Shikui Chen[1,*]
Department of Mechanical Engineering [1]
Department of Surgery [2]
Department of Neurological Surgery [3]
Department of Computer Science [4]
Department of Applied Mathematics & Statistics [5]
State University of New York at Stony Brook, Stony Brook, New York, USA, 11794
Email: {Ran.Zhuang, Jiawei.Tian, Shikui.Chen, Xianfeng.Gu}@stonybrook.edu;
{Apostolos.Tassiopoulos, Chandramouli.Sadasivan}@stonybrookmedicine.edu

ABSTRACT

Minimally invasive endovascular therapy (MIET) is an innovative technique that utilizes percutaneous access and transcatheter implantation of medical devices to treat vascular diseases. However, conventional devices often face limitations such as incomplete or suboptimal treatment, leading to issues like recanalization in brain aneurysms, endoleaks in aortic aneurysms, and paravalvular leaks in cardiac valves. In this study, we introduce a new metastructure design for MIET employing re-entrant honeycomb structures with negative Poisson's ratio (NPR), which are initially designed through topology optimization and subsequently mapped onto a cylindrical surface. Using ferromagnetic soft materials, we developed structures with adjustable mechanical properties called magnetically activated structures (MAS). These magnetically activated structures can change shape under noninvasive magnetic fields, letting them fit against blood vessel walls to fix leaks or movement issues. The soft ferromagnetic materials allow the stent design to be remotely controlled, changed, and rearranged using external magnetic fields. This offers accurate control over stent placement and positioning inside blood vessels. We performed magneto-mechanical simulations to evaluate the proposed design's performance. Experimental tests were conducted on prototype beams to assess their bending and torsional responses to external magnetic fields. The simulation results were compared with experimental data to determine the accuracy of the magneto-mechanical simulation model for ferromagnetic soft materials. After validating the model, it was used to analyze the deformation behavior of the plane matrix and cylindrical structure designs of the Negative Poisson's Ratio (NPR) metamaterial. The results indicate that the plane matrix NPR metamaterial design exhibits concurrent vertical and horizontal expansion when subjected to an external magnetic field. In contrast, the cylindrical structure demonstrates simultaneous axial and radial expansion under the same conditions. The preliminary findings demonstrate the considerable potential and practicality of the proposed methodology in the development of magnetically activated MIET devices, which offer biocompatibility, a diminished risk of adverse reactions, and enhanced therapeutic outcomes. Integrating ferromagnetic soft materials into mechanical metastructures unlocks promising opportunities for designing stents with adjustable mechanical properties, propelling the field towards more sophisticated minimally invasive vascular interventions.

[*]Address all correspondence to this author.

1 INTRODUCTION

Minimally invasive endovascular therapy involves the percutaneous access and transcatheter implantation of medical devices for treating vascular diseases throughout the body. Brain aneurysms, aortic aneurysms, and cardiac valve replacement are the three most prominent segments in the global endovascular market, with a combined worth of at least USD 6.5 billion [1, 2, 3]. The primary limitation of available devices, such as stents and coils for brain aneurysms, stent grafts for aortic aneurysms, and stent valves for aortic valves, is incomplete or non-optimal treatment, leading to recanalization in brain aneurysms [1], endoleaks in aortic aneurysms [2], and paravalvular leaks in cardiac valves [3]. These issues arise from poor device-structure fit to the patient anatomy, resulting in improper scaffold for vascular remodeling around the implanted device and device migration, primarily for aortic aneurysms and cardiac valves.

Abdominal aortic aneurysms (AAA) are fusiform dilations of the abdominal aorta affecting about 3% of the population over 50 [1]. EVAR is the preferred treatment modality in most patients with suitable anatomy and reasonable life expectancy, with about 80% of AAA cases currently treated by EVAR [4]. However, clinical benefits of EVAR are lost relative to open surgery over the long term due to endoleaks, graft displacement, limb occlusions, stent fractures, and secondary ruptures, requiring retreatment in 20-25% of patients on average [5, 6, 7, 8, 9].

To address the limitations of traditional EVAR treatment, this study leverages soft active structures to optimize and enhance the procedure. The inherent flexibility of soft materials allows for increased range and mobility. Nowadays, soft active materials are adopted widely in various fields, including soft robots [10, 11, 12, 13], compliant electronics [14, 15, 16] and biomedical devices [17, 18, 19]. Among the different methods used to actuate soft active materials [20, 21, 22, 23], the magnetic field stands out due to several advantages. Firstly, magnetic fields offer fast and contactless stimuli to control soft magnetic materials, making them safe for biomedical applications [24]. Secondly, magnetic fields can generate relatively higher force and torque in soft magnetic structures, resulting in large displacement fields [25]. Moreover, soft magnetic materials can be programmed to achieve complex deformation and magnetic particle magnetization, making them versatile for various applications [20]. Magnetically activated structures traditionally utilize iron or iron oxide particles embedded in polymers. Those particles have low coercivity, as shown in Fig.1(a), which generates high magnetization with a magnetic field applied and doesn't preserve much magnetization once the external magnetic field is removed [26, 27, 28]. Therefore, the low-coercivity soft material could only generate tension and compression. On the other hand, ferromagnetic material with high coercivity, as shown in Fig.1(b), could preserve high residual magnetic flux density. With the tendency of being parallel to an external magnetic field, the residual magnetic

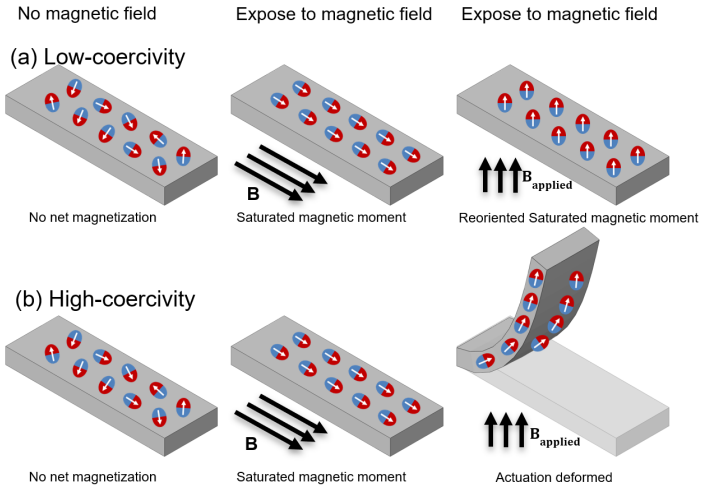

FIGURE 1: A schematic beam model for illustrating the magnetic deformation. (a) Magnetization in a beam made of low-coercivity particles. (b) Magnetization in a beam made of high-coercivity particles.

flux density generates torque, causing bending or torsion deformation on the ferromagnetic soft material. The particles, such as NdFeB powder, are commonly applied for high-coercivity ferromagnetic material to reach complicated deformation field [29, 30, 20]. By leveraging this physical property, many researchers have designed and fabricated these ferromagnetic soft robots [20, 24, 31, 32, 33].

To enhance and optimize EVAR treatment, we aim to develop novel magnetically activated structures (MAS) containing high-coercivity materials. The noninvasive magnetic field can deform the magnetically activated structures grafts, enabling them to conform to the vascular wall, thereby mitigating leaks or migrations. Furthermore, any graft displacement during the follow-up period can be corrected by noninvasively repositioning the devices.

This paper presents a new stent design for minimally invasive endovascular therapy that incorporates ferromagnetic soft materials into mechanical metastructures to create MAS with controllable and tunable mechanical properties. The integration of these materials into the stent design allows for remote actuation, deformation, or reconfiguration by applying an external magnetic field. This enables precise control over stent deployment and positioning within the vasculature, which is critical in achieving optimal therapeutic outcomes. Moreover, these metastructures can be designed to be biocompatible, minimizing the risk of adverse reactions and improving patient outcomes. The proposed pairing of metastructures with embedded ferromagnetic soft materials in stent design can provide a promising approach to developing minimally invasive endovascular therapy devices with improved efficacy and patient outcomes.

The paper is structured as follows: Section 2 presents the

modeling of ferromagnetic soft materials, followed by Section 3 which introduces a smart metastructure design comprising ferromagnetic soft materials. The design includes the synthesis of NPR metamaterial by topology optimization, simulation of metamaterial under mechanical stimulation, and simulation of the magneto-mechanical performance of 2D metastructure and wrapped 3D cylindrical metastructure under a magnetic stimulus. Section 4 presents experimental validation, which involves fabricating four benchmark prototypes of ferromagnetic soft beams with different magnetization directions. The bending and torsion of these prototypes under a specific external magnetic field are compared with the magneto-mechanical simulation. Finally, Section 5 provides the concluding remarks and outlines future research directions.

2 MAGNETOMECHANICAL MODEL for FERROMAGNETIC SOFT MATERIALS

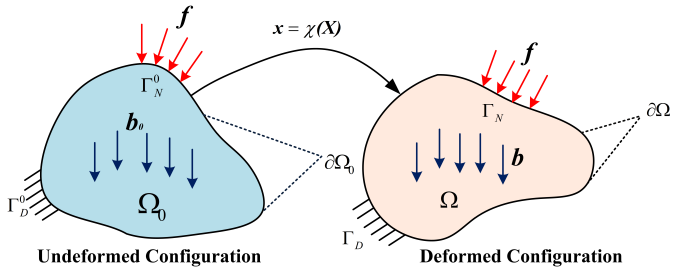

FIGURE 2: Transition from undeformed state to deformed state.

To provide a comprehensive overview, this section includes a brief kinematic description of how ferromagnetic soft materials respond to an applied magnetic field and undergo significant deformation. Interested readers can find more details in [34]. As depicted in Figure 2, the ferromagnetic soft body undergoes a substantial transformation from its initial undeformed state at $t = 0$ to its deformed state at time t. The mapping χ establishes a relationship between the positions of the undeformed state $\boldsymbol{X}$ in the reference frame and the deformed state position $\boldsymbol{x}$ in the spatial frame. The displacement can be calculated as $\boldsymbol{u} = \boldsymbol{x} - \boldsymbol{X}$. The deformation gradient tensor $\boldsymbol{F}$, can be calculated as,

$$\boldsymbol{F} = \frac{\partial \boldsymbol{x}}{\partial \boldsymbol{X}} = \frac{\partial(\boldsymbol{u}+\boldsymbol{X})}{\partial \boldsymbol{X}} = \boldsymbol{I} + \nabla_0 \boldsymbol{u}, \tag{1}$$

where $\boldsymbol{I}$ is the identity tensor, and ∇_0 denotes the gradient to the reference frame. The determinant of the deformation gradient is the deformation Jacobian, denoted as $J = det(\boldsymbol{F})$.

For pure elastic deformation of ferromagnetic soft material, a generalized neo-Hookean model is adopted, and the potential energy densityW_{E0} in the reference frame can be calculated as

$$W_{E0} = \frac{\mu}{2}\left(J^{-\frac{2}{3}} I_1 - 3\right) + \frac{1}{2} K (J-1)^2, \tag{2}$$

where μ and K are the shear and bulk modulus, respectively. The invariant is defined as $I_1 = trace(\boldsymbol{F}^T \mathbf{F})$.

When subjected to an external magnetic field $\boldsymbol{B}$, the soft material possesses magnetization or magnetic moment density $\boldsymbol{M}$ in the reference configuration, and its deformed state in the current configuration is $J^{-1}\boldsymbol{FM}$. Thus, we can calculate the current magnetic potential energy density as

$$W_M = J^{-1}\boldsymbol{FM} \cdot \boldsymbol{B}. \tag{3}$$

According to the relation $W_{M0} = JW_M$, the magnetic potential energy density in the reference frame can be written as

$$W_{M0} = \boldsymbol{FM} \cdot \boldsymbol{B}. \tag{4}$$

Thus, a combined potential energy density of ferromagnetic soft material in the reference frame can be expressed as

$$W_0 = \frac{\mu}{2}\left(J^{-\frac{2}{3}} I_1 - 3\right) + \frac{1}{2} K (J-1)^2 - \boldsymbol{FM} \cdot \boldsymbol{B}. \tag{5}$$

Based on the potential energy density function, it is straightforward to derive the first Piola-Kirchhoff stress as follows,

$$\begin{aligned} \boldsymbol{P} =& \frac{\partial W_0}{\partial \boldsymbol{F}} \\ =& \mu J^{-\frac{2}{3}}\left(\boldsymbol{F} - \frac{I_1}{3}\boldsymbol{F}^{-T}\right) + KJ(J-1)\boldsymbol{F}^{-T} - \boldsymbol{B} \otimes \boldsymbol{M}. \end{aligned} \tag{6}$$

In the above equation, the operator $\otimes$ is the dyadic product, in which two vectors can yield a second-order tensor. Next, the fourth-order material constitutive tensor based on the first Piola-Kirchhoff stress can be derived as

$$\begin{aligned} C_{ijkl} =& \frac{\partial P_{ij}}{\partial F_{kl}} \\ =& -\mu J^{-\frac{2}{3}}\left(\frac{2}{3}F_{ij}F^{-1}_{lk} - \frac{2}{9}I_1 F^{-1}_{ji}F^{-1}_{lk} - \delta_{ij}\delta_{jl}\right) \\ &+ \mu J^{-\frac{2}{3}}\left(-\frac{2}{3}F_{kl}F^{-1}_{ji} + \frac{I_1}{3}F^{-1}_{li}F^{-1}_{jk}\right) \\ &+ KJ\left((2J-1)F^{-1}_{ji}F^{-1}_{lk} - (J-1)F^{-1}_{li}F^{-1}_{jk}\right). \end{aligned} \tag{7}$$

3 METASTRUCTURE WITH EMBEDDED FERROMAGNETIC SOFT ACTUATORS

This section utilizes a re-entrant honeycomb NPR metamaterial structure, which can be systematically designed through topology optimization [35]. Mechanical simulations of the metamaterial structure are then performed for the unit cell, 2D array, and 3D cylinder shell. The NPR ferromagnetic metastructures are subjected to an applied magnetic field to actuate their response.

3.1 Designing Negative Poisson's Ratio (NPR) Metamaterials by Topology Optimization

Negative Poisson's ratio (NPR) metamaterials exhibit a unique property known as auxeticity. These materials are engineered at the micro or mesoscale with a specific geometric structure that allows them to expand in the direction perpendicular to the applied force. As a result, they can conform to freeform surfaces without developing wrinkles or other deformities, making them highly desirable for various applications. In particular, they have potential use in developing biomedical devices, advanced materials for aerospace and defense, and other areas where conformability to complex surfaces is critical. In this paper, we aim to map a 2D metamaterial design onto a cylinder to achieve radial expansion. Given that displacement in the axial direction is relatively easy to accomplish in a cylindrical shell structure, the NPR property is essential to convert axial displacement into radial displacement.

The present study utilizes a level-set-based topology optimization (TO) approach to design a mechanical metamaterial with a desired negative Poisson's ratio (NPR) [35]. To establish a relationship between the geometric configuration of cellular structures at the micro or mesoscale and the effective properties at the macro scale, the strain energy-based method [36] and the homogenization theory [37] are employed.

The constitutive of stress $\overline{\sigma}_{ij}$ and strain $\overline{\varepsilon}_{kl}$ for 2D isotropic material can be expressed as:

$$\begin{bmatrix} \overline{\sigma}_{11} \\ \overline{\sigma}_{22} \\ \overline{\sigma}_{12} \end{bmatrix} = \begin{bmatrix} C^H_{1111} & C^H_{1122} & 0 \\ C^H_{1122} & C^H_{2222} & 0 \\ 0 & 0 & C^H_{1212} \end{bmatrix} \begin{bmatrix} \overline{\varepsilon}_{11} \\ \overline{\varepsilon}_{22} \\ \overline{\varepsilon}_{12} \end{bmatrix}. \tag{8}$$

As a homogeneous medium, the strain energy of the unit cell can be constructed as follows:

$$U^H = \frac{1}{2} V \overline{\sigma}_{ij} \overline{\varepsilon}_{jk} = \frac{1}{2} \int_V \sigma_{ij} \varepsilon_{jk} dV. \tag{9}$$

By applying the uniform strain boundary condition given in Fig.3, the homogeneous elastic stiffness constants C^H_{1111}, C^H_{2222}, and C^H_{1122} can be expressed in terms of strain energy U^H_{1111}, U^H_{2222}, and U^H_{1122} as follows:

$$C^H_{1111} = 2U^H_{1111}. \tag{10}$$

$$C^H_{2222} = 2U^H_{2222}. \tag{11}$$

$$C^H_{1122} = U^H_{1122} - U^H_{1111} - U^H_{2222}. \tag{12}$$

The NPR material design problem can be formulated as a prob-

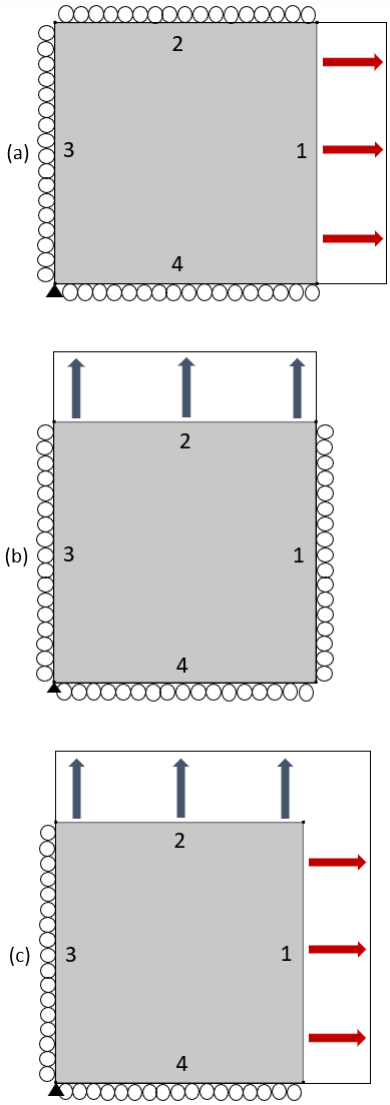

FIGURE 3: Boundary conditions for the unit cell: (a) Loading case 1, (b) Loading case 2, (c) Loading case 3.

lem to minimize the least square error between the homogenized elastic constants C^H_{ijkl} and the predicted homogenized elas-

tic constants C^*_{ijkl} as follows:

$$\textit{Minimize:} \quad J = \frac{1}{2} \sum_{i,j,k,l=1}^{2} w_{ijkl} \left(C^H_{ijkl} - C^*_{ijkl} \right)^2. \qquad (13)$$

With the target elastic stiffness constant set as C^*_{1111}=0.1 GPa, C^*_{2222}=0.1 GPa, and C^*_{1122}=-0.05 GPa. the structure is optimized and post-processed into a 4-by-$\sqrt{3}$ mm re-entrant honeycomb, as shown in Fig.4 (a). The re-entrant honeycomb unit cell is arrayed into a 10-by-10 matrix, as shown in Fig.4 (b). And then the matrix is wrapped into 3d cylinder shell, illustrated in Fig.4 (c).

The re-entrant honeycomb structure was selected due to its comparatively straightforward mechanical behavior, as illustrated in Fig.4. Specifically, when subjected to vertical loading, the oblique diagonal beams within the structure undergo rotational motion, causing the edges on the left and right sides to experience horizontal displacement.

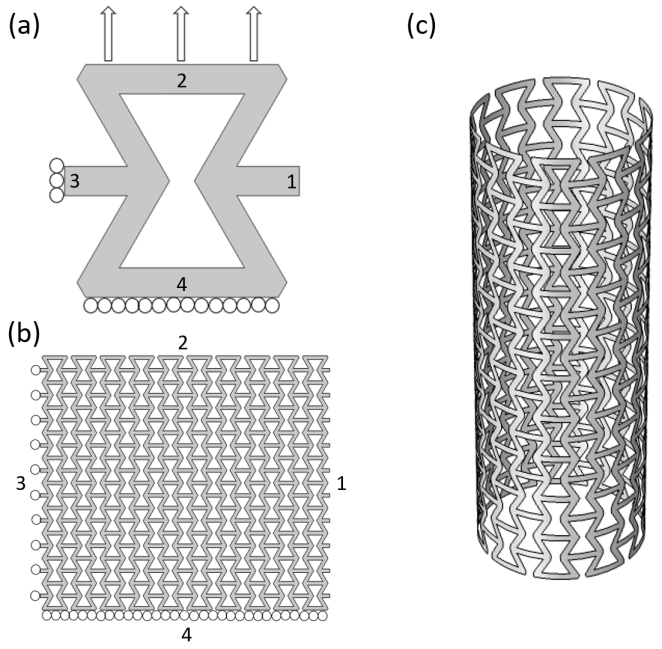

FIGURE 4: Boundary conditions for the re-entrant honeycomb unit structure and its planar and cylindrical assembly. (a) Unit cell with roller boundary conditions on edge 3 and edge 4, and 20% upward displacement on edge 2. (b) 2D hierarchical covalent array subjected to identical boundary conditions on edge 3 and edge 4, and 20% upward displacement on edge 2. (c) 3D hierarchical covalent array with fixed constraints at the bottom surface and 20% upward axial displacement at the top surface.

3.2 Mechanical Simulation of NPR Structure

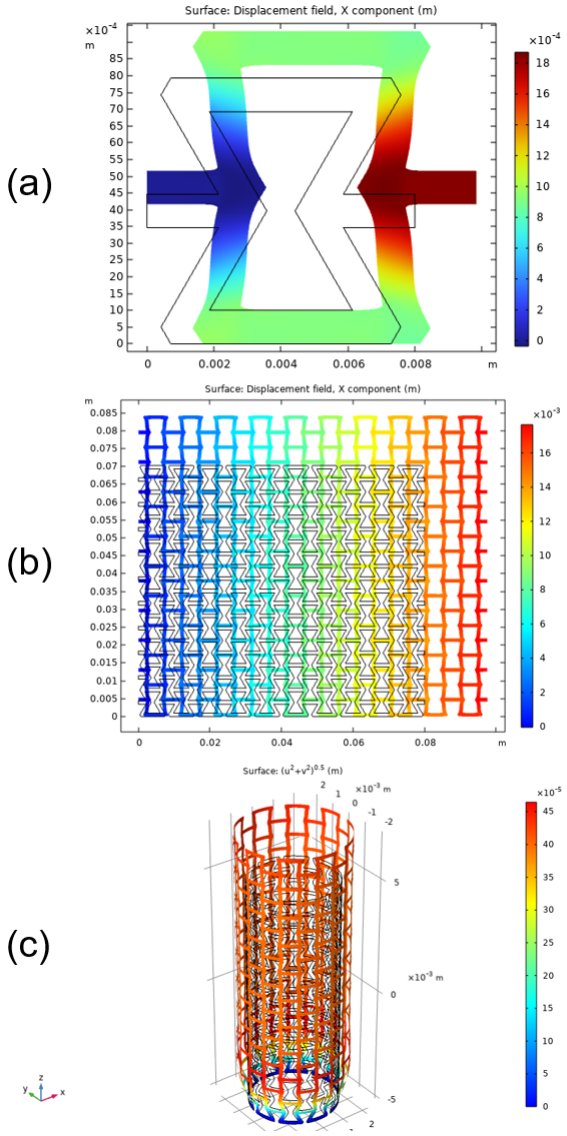

FIGURE 5: Mechanical simulation result of the re-entrant honeycomb unit structure, and its planar and cylindrical assembly. (a) Unit cell displacement field in the x direction. (b) Planar array structure displacement field in the x direction. (c) 3D hierarchical covalent array displacement field in radial direction

Analysis of re-entrant honeycomb allows predicting the Poisson's ratio for individual unit cells, 2D array, and 3d cylinder. A 4-by-$\sqrt{3}$ mm unit cell is analyzed for individual cells, and a 10-by-10 matrix is analyzed for an array of cells. The boundary conditions applied to 2D unit cell and 2D array structures are the roller constraint on edges 3 and 4, and the 20% of height displacement in the vertical direction on edge 2, depicted in Fig.4.

The resulting displacement in the x-direction on edge 1 is 20% of width for both individual unit cells and arrayed cells, indicated in Fig.5 (a) (b), and the Poisson's ratio of the re-entrant honeycomb is -1 for 2D cases.

In the simulation of the cylinder, the boundary condition applied is 20% of the height prescribed displacement in the axial direction of the cylinder's top end and fixed boundary to the cylinder's bottom end. The resulting displacement in the radial direction is 20% of the radius, shown in Fig.5 (c). The re-entrant honeycomb metamaterial keeps its negative Poisson's ratio on the 3d cylinder shell structure. The radius of the cylinder increases as the displacement is applied on the top surface.

3.3 Magneto-Mechanical Simulation on 2D Array

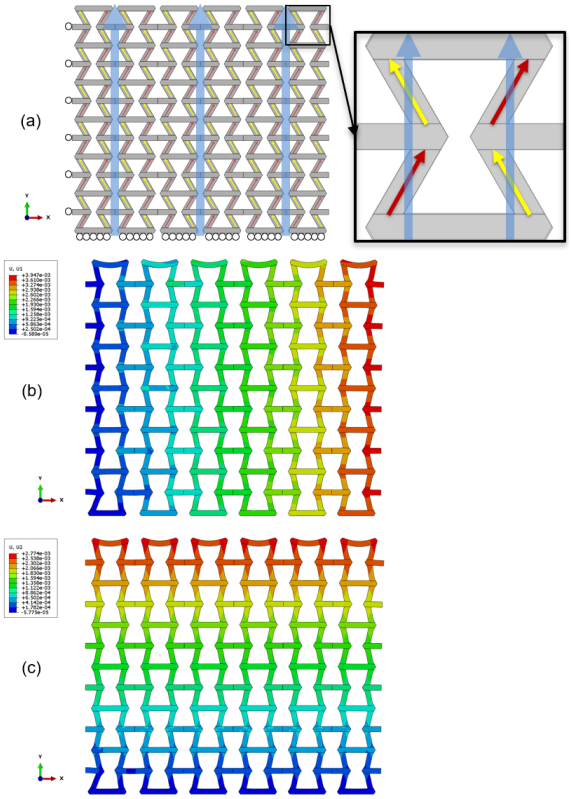

FIGURE 6: The 6-by-6 cell matrix boundary conditions and displacement fields driven by the magnetic field. (a) The roller boundary conditions of the simulation. (b) The displacement in the x direction. (c) The displacement in the y direction.

With the consistency of negative Poisson's ratio when mapping the re-entrant metamaterial matrix on a 3D cylinder, a 6-by-6 matrix made of 8-by-4$\sqrt{3}$ by 1 mm solid unit cell is driven by magnetic field instead of displacement on one end, discussed in 3.2. The roller boundary condition is applied on the left and bottom surfaces of the metamaterial matrix. The soft material has a shear modulus of 3e5 Pa and a bulk modulus of 3e8 Pa. Next, the multi-material ferromagnetic soft structure with different uniform magnetization directions [38] is introduced here to design the unit cell. In each unit cell shown in Fig.6, the left bottom and right top oblique diagonal beams in each unit cell have residual magnetic flux density pointing to the right top, whose magnetic moment density is 1.0×10^6 A/m in the x direction and 1.732×10^6 A/m in the y direction. The left top and right bottom of oblique diagonal beams in each unit cell have residual magnetic flux density pointing to the left top, whose magnetic moment density is -1.0×10^6 A/m in the x direction and 1.732×10^6 A/m in the y direction. The external magnetic field points upward with a magnetic field equal to 0.04 Tesla. The oblique diagonal beams are expected to align with the direction of the external magnetic field then the cell matrix would expand horizontally. A finite element environment in the forms of Abaqus/Standard use-element subroutine is employed to simulate the magnetically induced large deformation of ferromagnetic soft materials [20].

The resulting displacement in the x-direction on the right side equals 3.95 mm, indicated in Fig.6 (b), which is about 8.2% of the width. The resulting displacement in the y direction on the top edge equals 2.77 mm indicated in Fig.6 (c), which is about 6.6% of the width.

With different Magnetic fields applied to the 2D array of the structure, the maximum displacement increases, as shown in Fig.7.

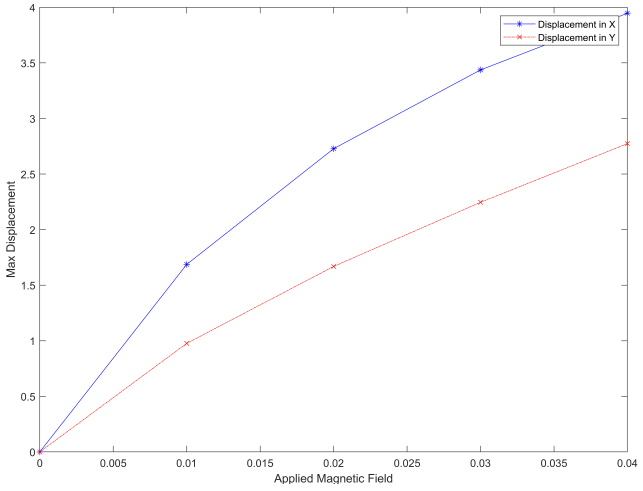

FIGURE 7: Maximum displacement in x and y direction vs applied magnetic field

3.4 Magneto-Mechanical Simulation on 3D Cylinder

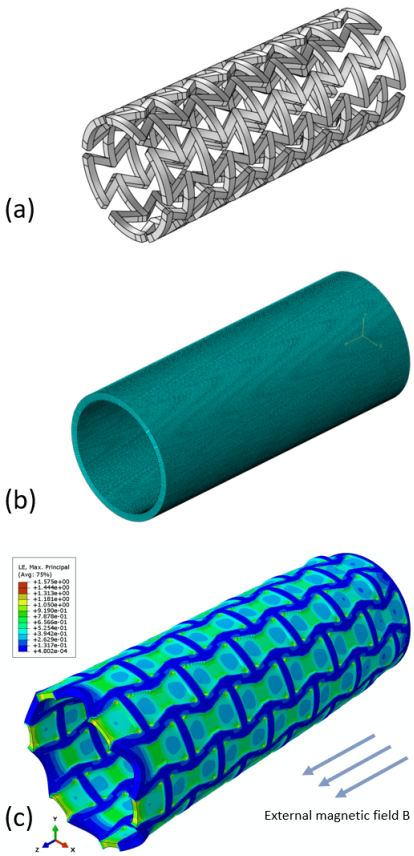

FIGURE 8: The wrapped 6-by-6 cylinder matrix. (a) CAD model of 6 layers. (b) The mesh of cylinder. (c) Logarithmic strain field. The external magnetic field B is applied in the z direction.

In section 3.2, it was demonstrated that the re-entrant honeycomb structure can induce the NPR property under mechanical expansion in the vertical direction and that this property is preserved when the structure is wrapped into a cylinder. To further investigate this, a 2D re-entrant honeycomb array was simulated under an external magnetic field in the previous section. The resulting 6x6 2D array structure was then wrapped into a 3D cylinder shell and simulated under the same magnetic field, as shown in Fig. 8(a).

Due to difficulties in meshing the structure as shown in Fig. 8(a), with C3D8 elements, a simplified cylinder shell with a weak material was introduced into the finite element analysis. This simplified shell has the same dimensions as the original cylinder. We substituted the air regions in the original structure with a weak material that has a low bulk modulus of 3e2 Pa and a low shear modulus of 3e5 Pa which are 0.1% of the soft material's shear and bulk modulus, and zero magnetization. The simplified shell is meshed into 300 by 300 elements on the cylindrical shell, as shown in 8(b).

The magnetization was then wrapped into cylindrical coordinates. The oblique diagonal beams, whose magnetic moment density was 1.0 × 106 A/m in the x direction and 1.732 × 106 A/m in the y direction, were transformed to 1.0 × 106 A/m in the tangent direction and 1.732 × 106 A/m in the z direction. Similarly, the oblique diagonal beams, whose magnetic moment density was -1.0 × 106 A/m in the x direction and 1.732 × 106 A/m in the y direction, were converted to -1.0 × 106 A/m in the tangent direction and 1.732 × 106 A/m in the z direction.

The resulting cylindrical structure shell was deformed subject to an encastre boundary condition on one end, while an external magnetic field of 0.04 Tesla was applied in the z direction. The resulting displacement in the radial direction was 1.1 mm, as shown in 8(c), which corresponds to 14.4% of the original radius. The resulting displacement in the axial direction on the unfixed end was 5.8% of the original length, also shown in 8(c).

4 Experiment of Beam's Bending and Torsion

In this section, the magneto-mechanical simulation is verified by comparing the experiment prototype result and the simulation result of a magnetized ferromagnetic beam under an external magnetic field. Beams with 4 different directions and their deformation under an applied external magnetic field are compared in this section.

4.1 Manufacturing of Ferromagnetic Soft Beam

The mold for 15-by-5-by-1.5 mm beams is 3d printed as shown in Fig.9 (a-b). The magnetic beam prototype is made of NdFeB powder and Ecoflex 00-30 rubber, which is a two-part, room-temperature curing silicone rubber. 20% volume percentage of NdFeB powder, 40% volume percentage of Ecoflex rubber part A and 40% volume percentage of Ecoflex rubber part B are prepared for the molding process, shown in Fig.9 (c). All parts are poured into a container and stirred by a stick, shown in Fig.9 (d). The mixture is then degassed under at least 28 inches of vacuum to mitigate air bubbles shown in Fig.9 (e). Finally, the mixture is poured into the mold, shown in Fig.9 (f). After 5 hours of curing, the solidified model is taken out from the molds.

A holder was 3d printed, displayed in Fig.10 (a) to secure the beams in an IM-10-30 Impulse Magnetizer during magnetization. Four beams are magnetized, illustrated in Fig.10 (a); two of them have residual magnetic flux density in the length direction, and two of them have residual magnetic flux density in the width direction. Under the external magnetic field in the height direction, the beams with different magnetization, indicated in Fig.11 (a-d), are deforming in the direction shown in Fig.11 (i-l).

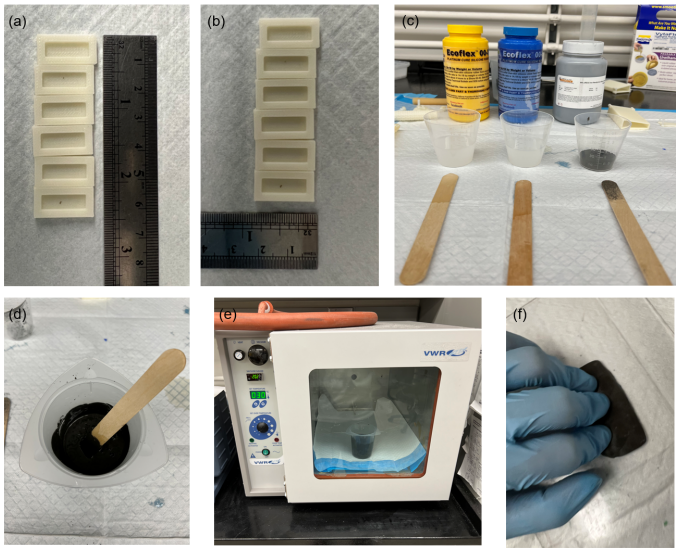

FIGURE 9: Experiment steps. (a-b) the mold for curing the beam. (c-d) 15 ml of NdFeB powder, 30 ml of Ecoflex 00-30 part A and 30 ml of Ecoflex 00-30 part B are prepared and mixed. (e) VWR vacuum machine is applied to eliminate the bubble in the mixture liquid. (f) the liquid is poured in to mold and cured for 5 hours.

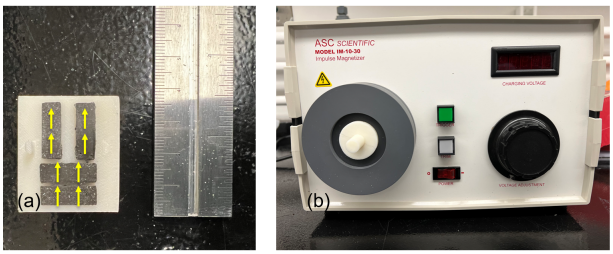

FIGURE 10: Ferromagnetic beam magnetization. (a) The beam is placed in the 3d printed holder, with yellow indicating the residual magnetic flux density of four beams after the magnetization process. (b) The model IM-10-30 Impulse Magnetizer used for the magnetization process.

4.2 Magneto-Mechanical Simulation and Comparison of Beam's Bending and Torsion

The deformation of the manufactured beam under external magnetic is compared with the magneto-mechanical simulation of the ferromagnetic beam to verify the simulation model. During the simulation, the residual magnetic flux density directions of the ferromagnetic beam are oriented in the positive and negative x, as well as positive and negative z directions, indicated by yellow arrows in Fig.11 (a-d). The left end is affixed with encastre boundary conditions. An external magnetic field was applied in the y direction to induce deformation, as shown in the blue arrow in Fig.11 (a-d). The resulting displacement of simulation, depicted in Fig.11 (e-h), is consistent with the deformation

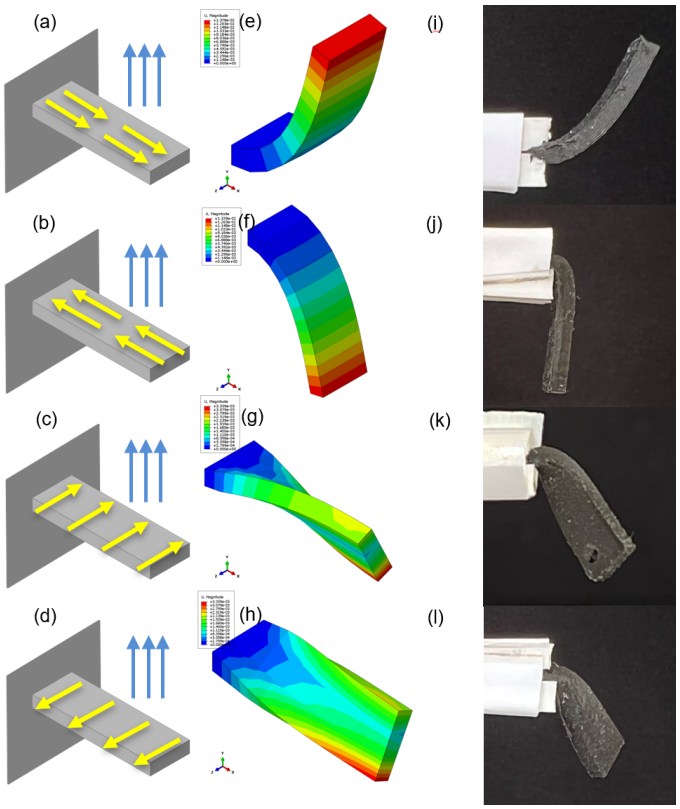

FIGURE 11: The deformation of beam numerical result and prototype under external magnetic field in the y direction. (a-d) The residual magnetic flux density directions are shown in the yellow arrow direction. The external magnetic field is shown in the blue arrow direction. (e-h) The simulation result of beams' displacement magnitude with corresponding residual magnetic flux density directions is shown in a-d. (i-l) The beam prototypes' displacement with corresponding residual magnetic flux density directions are shown in a-d.

of the beam manufactured 11 (i-l). The deformation directions of the ferromagnetic beam indicate that the beam bent in the direction where the magnetization of the material aligned with the external magnetic field.

5 CONCLUSION

This study proposes using magnetically activated structures carrying high-coercivity materials to expand the stent radially and optimize endovascular aneurysm repair treatment. To make the stent conform to the complex geometry of the vessel and facilitate design, the authors employ re-entry negative Poisson's ratio metamaterial. The NPR property of the calculated re-entry honeycomb metamaterial is then simulated on a unit cell and 2D array before being wrapped in a 3D cylinder shell. The simulation results indicate that the NPR property is retained after the

shape transformation. To simulate the deformation of the NPR magnetically activated 2D structure, the authors use the magneto-mechanical model for ferromagnetic soft materials, which expands both vertically and horizontally under a vertical magnetic field. This 2D structure has been wrapped in a 3D cylindrical shell. Subsequently, the magneto-mechanical model is applied to simulate the deformation of the 3D cylindrical shell, which indicates that the cylinder expands both radially and axially under an axial magnetic field.

Additionally, four ferromagnetic soft beams, with different magnetization, are fabricated and deformed under an external magnetic field. The bending and torsion of the ferromagnetic beam under a magnetic field are consistent with the simulation result. Both experiment and simulation agree with the fact that residual magnetic flux density has a propensity for aligning to the applied magnetic field.

Future work aims to design a cylindrical ferromagnetic NPR metamaterial structure with zero Poisson's ratio, which expands only in a radial direction under a uniform axial magnetic field. Furthermore, our further research could work on the fabrication of conformable ferromagnetic soft meta-structures and employ topology optimization to design stents for more complicated deformation.

ACKNOWLEDGMENT

The authors gratefully acknowledge financial support from NIH through grant R21EB029733, the National Science Foundation through grants CMMI-1762287 and PFI-RP-2213852, and the State University of New York (SUNY) at Stony Brook through the Summer 2022 OVPR Seed Grant 93214.

REFERENCES

[1] Tan, I., Agid, R., and Willinsky, R. "Recanalization rates after endovascular coil embolization in a cohort of matched ruptured and unruptured cerebral aneurysms". *Interventional Neuroradiology,* ***17***(1), pp. 27–35.

[2] Hori, D., Nomura, Y., Yamauchi, T., Furuhata, H., Matsumoto, H., Kimura, N., Yuri, K., and Yamaguchi, A. "Perioperative factors associated with aneurysm sac size changes after endovascular aneurysm repair". *Surgery Today,* ***49***, pp. 130–136.

[3] Gopalakrishnan, D., Gopal, A., and Grayburn, P. A. Evaluating paravalvular leak after TAVR.

[4] Patel, R., Sweeting, M. J., Powell, J. T., and Greenhalgh, R. M. "Endovascular versus open repair of abdominal aortic aneurysm in 15-years' follow-up of the UK endovascular aneurysm repair trial 1 (EVAR trial 1): a randomised controlled trial". *The Lancet,* ***388***(10058), pp. 2366–2374.

[5] Zoethout, A. C., Boersen, J. T., Heyligers, J. M., de Vries, J.-P. P., Zeebregts, C. J., and Reijnen, M. M. "Two-year outcomes of the Nellix endovascular aneurysm sealing system for treatment of abdominal aortic aneurysms". *Journal of Endovascular Therapy,* ***25***(3), pp. 270–281.

[6] Quinn, A. A., Mehta, M., Teymouri, M. J., Keenan, M. E., Paty, P. S., Zhou, Y., Chang, B. B., and Feustel, P. "The incidence and fate of endoleaks vary between ruptured and elective endovascular abdominal aortic aneurysm repair". *Journal of vascular surgery,* ***65***(6), pp. 1617–1624.

[7] van Marrewijk, C., Buth, J., Harris, P. L., Norgren, L., Nevelsteen, A., and Wyatt, M. G. "Significance of endoleaks after endovascular repair of abdominal aortic aneurysms: the EUROSTAR experience". *Journal of vascular surgery,* ***35***(3), pp. 461–473.

[8] Daye, D., and Walker, T. G. "Complications of endovascular aneurysm repair of the thoracic and abdominal aorta: evaluation and management". *Cardiovascular diagnosis and therapy,* ***8***(Suppl 1), p. S138.

[9] Goudeketting, S. R., Jin, P. P. F. K., Ünlü, Ç., and de Vries, J.-P. P. "Systematic review and meta-analysis of elective and urgent late open conversion after failed endovascular aneurysm repair". *Journal of vascular surgery,* ***70***(2), pp. 615–628.

[10] Wehner, M., Truby, R. L., Fitzgerald, D. J., Mosadegh, B., Whitesides, G. M., Lewis, J. A., and Wood, R. J. "An integrated design and fabrication strategy for entirely soft, autonomous robots". *Nature,* ***536***(7617), p. 451.

[11] Park, S.-J., Gazzola, M., Park, K. S., Park, S., Di Santo, V., Blevins, E. L., Lind, J. U., Campbell, P. H., Dauth, S., Capulli, A. K., et al. "Phototactic guidance of a tissue-engineered soft-robotic ray". *Science,* ***353***(6295), pp. 158–162.

[12] Kim, S., Laschi, C., and Trimmer, B. "Soft robotics: a bioinspired evolution in robotics". *Trends in biotechnology,* ***31***(5), pp. 287–294.

[13] Tian, J., Zhao, X., Gu, X. D., and Chen, S. "Designing ferromagnetic soft robots (FerroSoRo) with level-set-based multiphysics topology optimization". In 2020 IEEE International Conference on Robotics and Automation (ICRA), IEEE, pp. 10067–10074.

[14] Zarek, M., Layani, M., Cooperstein, I., Sachyani, E., Cohn, D., and Magdassi, S. "3D printing of shape memory polymers for flexible electronic devices". *Advanced Materials,* ***28***(22), pp. 4449–4454.

[15] Fan, J. A., Yeo, W.-H., Su, Y., Hattori, Y., Lee, W., Jung, S.-Y., Zhang, Y., Liu, Z., Cheng, H., Falgout, L., et al. "Fractal design concepts for stretchable electronics". *Nature communications,* ***5***, p. 3266.

[16] Ma, M., Guo, L., Anderson, D. G., and Langer, R. "Bio-inspired polymer composite actuator and generator driven by water gradients". *Science,* ***339***(6116), pp. 186–189.

[17] Zhao, X., Kim, J., Cezar, C. A., Huebsch, N., Lee, K., Bouhadir, K., and Mooney, D. J. "Active scaffolds for on-demand drug and cell delivery". *Proceedings of the National Academy of Sciences,* ***108***(1), pp. 67–72.

[18] Cianchetti, M., Laschi, C., Menciassi, A., and Dario, P. "Biomedical applications of soft robotics". *Nature Reviews Materials,* ***3***(6), pp. 143–153.

[19] Fusco, S., Sakar, M. S., Kennedy, S., Peters, C., Bottani, R., Starsich, F., Mao, A., Sotiriou, G. A., Pané, S., Pratsinis, S. E., et al. "An integrated microrobotic platform for on-demand, targeted therapeutic interventions". *Advanced Materials,* ***26***(6), pp. 952–957.

[20] Kim, Y., Yuk, H., Zhao, R., Chester, S. A., and Zhao, X. "Printing ferromagnetic domains for untethered fast-transforming soft materials". *Nature,* ***558***(7709), p. 274.

[21] Zhang, W., Ahmed, S., Masters, S., Ounaies, Z., and Frecker, M. "Finite element analysis of electroactive polymer and magnetoactive elastomer based actuation for origami-inspired folding". In ASME 2016 Conference on Smart Materials, Adaptive Structures and Intelligent Systems, American Society of Mechanical Engineers, pp. V001T01A001–V001T01A001.

[22] Brunet, T., Merlin, A., Mascaro, B., Zimny, K., Leng, J., Poncelet, O., Aristégui, C., and Mondain-Monval, O. "Soft 3D acoustic metamaterial with negative index". *Nature materials,* ***14***(4), p. 384.

[23] Grier, D. G. "A revolution in optical manipulation". *nature,* ***424***(6950), p. 810.

[24] Xu, T., Zhang, J., Salehizadeh, M., Onaizah, O., and Diller, E. "Millimeter-scale flexible robots with programmable three-dimensional magnetization and motions". *Science Robotics,* ***4***(29), p. eaav4494.

[25] Tian, J., Li, M., Han, Z., Chen, Y., Gu, X. D., Ge, Q., and Chen, S. "Conformal topology optimization of multi-material ferromagnetic soft active structures using an ex-

tended level set method". *Computer Methods in Applied Mechanics and Engineering,* ***389***, p. 114394.
[26] Chester, S. A., Di Leo, C. V., and Anand, L. "A finite element implementation of a coupled diffusion-deformation theory for elastomeric gels". *International Journal of Solids and Structures,* ***52***, pp. 1–18.
[27] Harne, R. L., Deng, Z., and Dapino, M. J. "Adaptive magnetoelastic metamaterials: A new class of magnetorheological elastomers". *Journal of Intelligent Material Systems and Structures,* ***29***(2), pp. 265–278.
[28] Evans, B., Shields, A., Carroll, R. L., Washburn, S., Falvo, M., and Superfine, R. "Magnetically actuated nanorod arrays as biomimetic cilia". *Nano letters,* ***7***(5), pp. 1428–1434.
[29] Lum, G. Z., Ye, Z., Dong, X., Marvi, H., Erin, O., Hu, W., and Sitti, M. "Shape-programmable magnetic soft matter". *Proceedings of the National Academy of Sciences,* ***113***(41), pp. E6007–E6015.
[30] Hu, W., Lum, G. Z., Mastrangeli, M., and Sitti, M. "Small-scale soft-bodied robot with multimodal locomotion". *Nature,* ***554***(7690), p. 81.
[31] Wu, S., Ze, Q., Zhang, R., Hu, N., Cheng, Y., Yang, F., and Zhao, R. "Symmetry-breaking Actuation Mechanism for Soft Robotics and Active Metamaterials". *ACS Applied Materials & Interfaces,* ***11***(44), pp. 41649–41658.
[32] Tian, J., Zhao, X., Gu, X. D., and Chen, S. "Designing Conformal Ferromagnetic Soft Actuators Using Extended Level Set Methods (X-LSM)". In International Design Engineering Technical Conferences and Computers and Information in Engineering Conference, Vol. 83990, American Society of Mechanical Engineers, p. V010T10A012.
[33] Zhao, Z., and Zhang, X. S. "Topology optimization of hard-magnetic soft materials". *Journal of the Mechanics and Physics of Solids,* ***158***, p. 104628.
[34] Zhao, R., Kim, Y., Chester, S. A., Sharma, P., and Zhao, X. "Mechanics of hard-magnetic soft materials". *Journal of the Mechanics and Physics of Solids,* ***124***, pp. 244–263.
[35] Vogiatzis, P., Chen, S., Wang, X., Li, T., and Wang, L. "Topology optimization of multi-material negative Poisson's ratio metamaterials using a reconciled level set method". *Computer-Aided Design,* ***83***, pp. 15–32.
[36] Zhang, W., Dai, G., Wang, F., Sun, S., and Bassir, H. "Using strain energy-based prediction of effective elastic properties in topology optimization of material microstructures". *Acta Mechanica Sinica,* ***23***(1), pp. 77–89.
[37] Hassani, B., and Hinton, E. "A review of homogenization and topology optimization I—homogenization theory for media with periodic structure". *Computers & Structures,* ***69***(6), pp. 707–717.
[38] Tian, J., Gu, X. D., and Chen, S. "Multi-material topology optimization of ferromagnetic soft robots using reconciled level set method". In International Design Engineering Technical Conferences and Computers and Information in Engineering Conference, Vol. 85451, American Society of Mechanical Engineers, p. V08BT08A014.